

Drylands face potential threat under 2 °C global warming target

Jianping Huang^{1*}, Haipeng Yu¹, Aiguo Dai^{2,3}, Yun Wei¹ and Litai Kang¹

The Paris Agreement aims to limit global mean surface warming to less than 2 °C relative to pre-industrial levels^{1–3}. However, we show this target is acceptable only for humid lands, whereas drylands will bear greater warming risks. Over the past century, surface warming over global drylands (1.2–1.3 °C) has been 20–40% higher than that over humid lands (0.8–1.0 °C), while anthropogenic CO₂ emissions generated from drylands (~230 Gt) have been only ~30% of those generated from humid lands (~750 Gt). For the twenty-first century, warming of 3.2–4.0 °C (2.4–2.6 °C) over drylands (humid lands) could occur when global warming reaches 2.0 °C, indicating ~44% more warming over drylands than humid lands. Decreased maize yields and runoff, increased long-lasting drought and more favourable conditions for malaria transmission are greatest over drylands if global warming were to rise from 1.5 °C to 2.0 °C. Our analyses indicate that ~38% of the world's population living in drylands would suffer the effects of climate change due to emissions primarily from humid lands. If the 1.5 °C warming limit were attained, the mean warming over drylands could be within 3.0 °C; therefore it is necessary to keep global warming within 1.5 °C to prevent disastrous effects over drylands.

After the Paris Climate Agreement was signed in April 2016 and approved by USA and China on the G20 summit in September 2016, policymakers agreed upon a goal to limit global mean surface warming (GMSW) to no more than 2 °C above pre-industrial levels¹. Furthermore, the pursuit of a warming limit as low as 1.5 °C was proposed and the Intergovernmental Panel on Climate Change (IPCC) was invited to generate a special report by 2018 on the impacts of global warming of 1.5 °C and on related global greenhouse gas emissions pathways. As part of an ambitious and urgent plan, the necessity and benefits of half a degree less warming must be evaluated soon before a new decision is made.

The GMSW level has already reached ~0.9 °C above the pre-industrial level⁴, leaving only ~0.6 °C for further warming before reaching a 1.5 °C target. Thus, it is suggested that a 1.5 °C target is not likely to be achieved without an overshoot, given recent CO₂ emissions trends². However, some studies found extreme temperature changes associated with the 2 °C target could be substantial and a 1.5 °C target may be desirable³.

These global warming targets are for global mean surface temperatures averaged over both land and ocean surfaces. Greenhouse gas (GHG)-induced warming is much lower over oceans than over land, owing to evaporation over and vertical mixing within oceans⁵. Thus, warming over land will significantly exceed the GMSW target due to the lower warming over oceans, which cover ~71% of Earth's surface.

Warming over land is also not evenly distributed, and large regional differences have raised concerns^{3,6–8}. Observations have shown enhanced warming over drylands^{9–11}. The world's drylands occupy nearly half of Earth's land surface and sustain ~38% of world's population. Drylands are at a high risk of land degradation and desertification, owing to their fragile ecosystems¹². Thus, it is important to examine changes across drylands under the 2 °C and 1.5 °C targets.

Historical warming trends as a function of mean precipitation (P) (Fig. 1a) are compared among three observational data sets: GISS, CRUTEM4 and MLOST (Methods), together with Fifth Coupled Model Intercomparison Project (CMIP5) all-forcing historical simulations¹³ (Supplementary Table 1; Methods). Here, we focus on the 1920–2015 period, because observations are sparse in many regions before 1920¹⁴. All three observational data sets show decreasing warming with increasing mean precipitation, indicating that warming has been more severe in dry areas, which is robust with different precipitation data sets (Methods) and periods (Supplementary Fig. 1). The distribution of drylands (here defined as land areas with mean annual precipitation (P) below 600 mm and the ratio of mean precipitation to potential evapotranspiration (P/PET)¹⁵ below 0.65, see Methods) is consistent with areas with high warming trends (Fig. 1b and Supplementary Fig. 2), and the mean temperature trend during 1920–2015 for drylands is 1.28 ± 0.18 °C/96 yr in MLOST (1.30 ± 0.19 °C/96 yr and 1.25 ± 0.19 °C/96 yr in CRUTEM4 and GISS, respectively). In contrast, the mean temperature trend for humid lands, defined as the areas with annual P > 600 mm and P/PET > 0.65, is 0.92 ± 0.13 °C/96 yr in MLOST (0.81 ± 0.14 °C/96 yr and 1.04 ± 0.14 °C/96 yr in CRUTEM4 and GISS, respectively), which is about 60% to 80% of the trend for drylands.

Anthropogenic CO₂ and other GHG emissions are considered to be the main cause of the recent global warming; however, CO₂ emissions from anthropogenic sources (Methods) over different land areas show a geographical pattern opposite to the warming patterns (Fig. 1). Drylands correspond to low total CO₂ emissions of ~4.58 kg m⁻² during 1920–2013, whereas humid lands generate high total CO₂ emissions ~15.43 kg m⁻², or approximately 3.5 times that of drylands—mainly from Europe, eastern North America and eastern Asia (Fig. 1c). This pattern is also robust over different periods (Supplementary Fig. 3). Atmospheric CO₂, a highly mixed GHG after emissions, is distributed uniformly across the globe, and surface temperatures over drylands are more sensitive to the CO₂ levels than other areas. In this case, although most of the global CO₂ emissions were geographically emitted from humid lands (~750 GtC from 1920–2013, 1 Gt = 10¹⁵ g, compared with the emissions of ~230 GtC from drylands), 20%–40% more warming occurred over drylands. This large asymmetry between the

¹Key Laboratory for Semi-Arid Climate Change of the Ministry of Education, College of Atmospheric Sciences, Lanzhou University, Lanzhou 730000, China. ²Department of Atmospheric & Environmental Sciences, State University of New York at Albany, New York 12222, USA. ³National Center for Atmospheric Research, PO Box 3000, Boulder, Colorado 80307-3000, USA. *e-mail: hjp@lzu.edu.cn

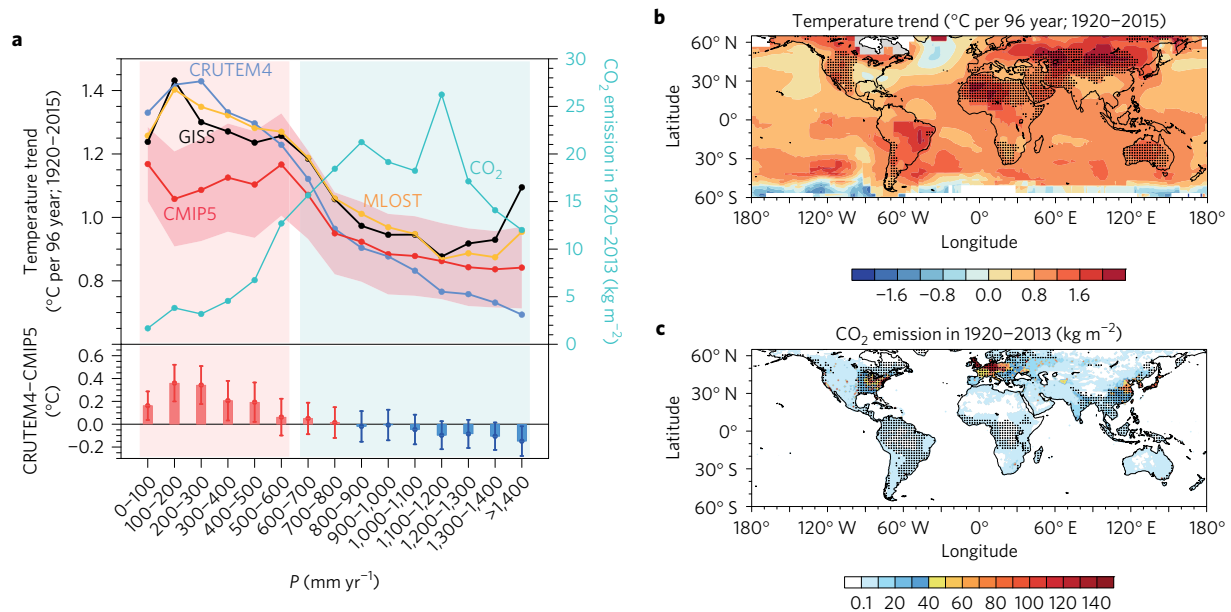


Figure 1 | Temperature trends and historical CO₂ emissions for drylands and humid lands. **a**, Variations in regionally averaged temperature trends from 1920–2015 (°C per 96 yr) calculated from the MLOST (yellow line), CRUTEM4 (blue line) and GISS (black line), and the ensemble mean of the CMIP5 simulations (red line), together with regionally averaged total CO₂ emissions flux during 1920–2013 (kg m⁻²) as a function of the climatological (1948–2005) mean precipitation from GPCP V6 over land surfaces. Bars denote the difference between regionally averaged CRUTEM4 temperature trends and the CMIP5 ensemble mean (CRUTEM4 minus CMIP5), and error bars and red shading denote the 95% confidence intervals for the 18 models. CMIP5 all-forcing historical simulations (for 1920–2005) and the RCP4.5 projections (for 2006–2015) were used. **b**, The global distribution of surface temperature trends for 1920–2015 from the MLOST, with the grey shading denoting the identified drylands. **c**, The global distribution of total CO₂ emissions flux during 1920–2013, with the grey shading denoting the identified humid lands.

geographic distributions of the CO₂ emissions and warming rates has not received much attention.

In addition to historical observations, the enhanced warming over drylands is expected to continue in the future. Surface warming over drylands is projected to reach ~6.5 °C (~3.5 °C) under the high RCP8.5 (low-moderate RCP4.5) emissions scenario by the end of this century (Supplementary Fig. 4). Although there are considerable spreads among the CMIP5 models, almost all of them show higher warming over drylands than humid lands (Supplementary Fig. 5). When GMSW reaches 2 °C (1.5 °C), mean warming over drylands should reach ~2.7 °C (~2.0 °C). However, Fig. 1a shows that the CMIP5 ensemble-mean dryland warming is only about 1.05 ± 0.17 °C/96 yr for 1920–2015, which is considerably less than that derived from the three observational data sets (the average is 1.28 ± 0.19 °C/96 yr). Thus, the CMIP5 models underestimate the historical warming over drylands (Fig. 1a), and the future warming over drylands could be more than that projected by CMIP5.

To further quantify the amplification of the warming over drylands, we compare (Fig. 2) the mean dryland temperature changes with the GMSW level for both observations and CMIP5 models. It is clear that the dryland warming rate is approximately 1.35 times that of the GMSW for both historical and future periods in the CMIP5 ensemble mean (Fig. 2a). However, the amplification in three observational data sets cannot be directly compared with that of the CMIP5 ensemble mean, because both externally forced changes and internally generated variations exist in the observational data, whereas the CMIP5 ensemble mean represents mostly forced changes¹⁶. We used the global-mean temperature series of the CMIP5 ensemble mean to regress against the observed temperature series at each grid point to derive an estimate of the forced component for each of the three observational data sets, with the residual taken as the unforced component¹⁴ (Methods). The ratio of the externally forced component averaged over drylands (humid lands) to that averaged over the globe is referred to as the externally

forced amplification, which is ~1.7 for drylands based on MLOST (~2.0 and ~1.6 using CRUTEM4 and GISS, respectively) (Fig. 2c). Extending this amplification factor of 1.6–2.0 to the future, dryland warming could be 3.2–4.0 °C (2.4–3.0 °C) when the GMSW reaches 2 °C (1.5 °C). Similarly, the externally forced amplification in humid lands is ~1.3 for the MLOST (~1.3 and ~1.2 for the CRUTEM4 and GISS, respectively), whereas the CMIP5 amplification in humid lands is ~1.2 (Fig. 2b,c). Thus, when the GMSW reaches 2 °C (1.5 °C), warming in humid lands could be 2.4–2.6 °C (1.8–2.0 °C). Similarly, amplification by the unforced component can also be calculated, and the difference is insignificant across different regions or data sets (Supplementary Figs 7 and 8). The results are very similar if additional model runs are included in deriving the forced signal (Supplementary Fig. 11).

The enhanced surface warming in drylands can be explained by surface and atmospheric processes (Fig. 3). Over drylands, low soil moisture content limits evaporation and low vegetation cover leads to low transpiration rates¹⁷, resulting in a low mean latent heat flux of 16.12 W m⁻² over drylands compared with 66.49 W m⁻² over humid lands (Fig. 3b) (Methods). Vegetation can lower air temperature via transpiration¹⁸ and by converting absorbed sunlight into chemical energy via photosynthesis¹⁹; thus, alleviating the extra heating from increased GHGs and resulting in low warming rates. This appears to be the case shown in Fig. 3c, which shows that surface warming rates decrease with increasing vegetation cover (Methods). To release the heating from solar and infrared radiation through sensible heat fluxes, surface temperatures over drylands must rise sharply to create a large land–air temperature gradient. This leads to a large sensible heat flux of 66.44 W m⁻² compared with that of 36.02 W m⁻² over humid lands (Fig. 3b). The high upward net longwave radiation over drylands of 79.33 W m⁻² (versus 50.82 W m⁻² over humid lands) also indicates a large land–air temperature difference over drylands. Therefore, the high sensitivity of surface temperatures to extra heating from increased

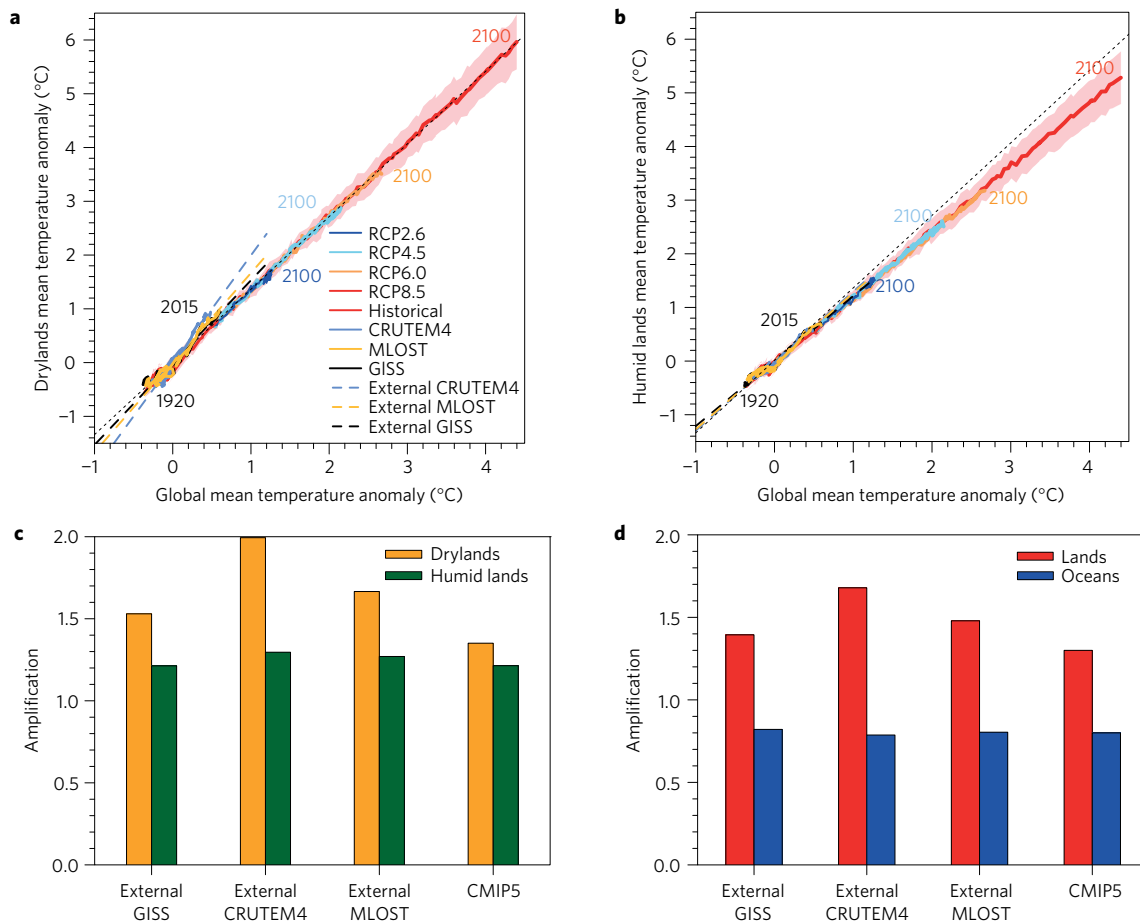


Figure 2 | The comparison of warming amplification over different regions based on CMIP5 and three observational data sets. a,b, Anomaly relationship between the mean global surface air temperature and that of (a) drylands and (b) humid lands based on the GISS, MLOST and CRUTEM4 data sets (after 5-year running averaging). Also shown are the estimated externally forced components in the data sets (dashed lines) and the ensemble mean of the CMIP5 historical simulations, RCP8.5, RCP6.0, RCP4.5, and RCP2.6 twenty-first-century projections (2006–2100). Shading denotes the 95% confidence interval for the 18 models. The black dotted line is the linear regression of the CMIP5 over drylands. **c,d**, The amplification factor of drylands and humid lands (c) and all land and ocean surfaces (d) from the ensemble mean of CMIP5 and the estimated externally forced components of the GISS, CRUTEM4 and MLOST data sets.

GHGs over drylands results mainly from limited soil moisture and vegetation, and any extra heating will be used to raise the surface temperature. In contrast, some of this extra heating can be used for evapotranspiration over humid land²⁰, thus decreasing the resultant surface warming. In addition, a dry surface has a lower specific heat than a wet surface, and the same amount of heating will cause a larger warming over drylands than over humid lands. The above physical processes could also be at work under GHG-induced warming in the future⁵.

Furthermore, there are different types of clouds over drylands and humid lands (Methods). Optically thick low clouds often exist in humid lands; they are efficient reflectors of sunlight, but their longwave warming effect is limited owing to their low cloud tops. These low clouds cool humid land surfaces. In contrast, low humidity leads to few clouds over drylands, which result in less reflection and scattering of the incoming sunlight. Thin cirrus clouds are the main cloud type found over drylands, which allow most sunlight to pass through but absorb infrared radiation from the surface and lower troposphere and radiate toward space at much lower temperatures²¹. Thus, cirrus clouds tend to warm dryland surfaces. Shortwave cloud radiative forcing is -21.92 W m^{-2} over drylands and -52.87 W m^{-2} over humid lands. The difference gives a net (longwave plus shortwave) cloud radiative forcing of -2.63 W m^{-2} over drylands and of -17.68 W m^{-2} over humid lands

(Fig. 3d). Thus, clouds tend to cool humid land surfaces much more than dryland surfaces. However, whether the clouds would contribute to the different sensitivity to GHG forcing over the two different regions will depend on how the clouds change in a warmer climate.

Finally, satellite records of aerosol optical depth (AOD) (Methods) show that more anthropogenic aerosols exist over humid lands than over drylands, although more dust aerosols are found in extremely arid drylands (Supplementary Fig. 13). These anthropogenic aerosols absorb and scatter sunlight, thus cooling the surface. In addition, the aerosols can increase cloud water content and thus cloud albedo, thereby further decreasing surface temperatures²² over humid lands. This may have contributed to the regional differences in historical warming rates (Fig. 1). Besides the above thermodynamic processes, some dynamical factors^{23–25} may also contribute to dryland warming.

The above analyses indicate that dryland warming would be considerably higher under a GMSW limit of 2°C compared with that under a goal of 1.5°C . The impacts of the warming difference in drylands between these two goals are significant in terms of agricultural, hydrological, drought and health outcomes²⁶ (Supplementary Tables 2 and 3) (Methods). Maize yields would decrease slightly over drylands if GMSW were to reach 1.5°C , but the yield reduction would be more significant with 2.0°C

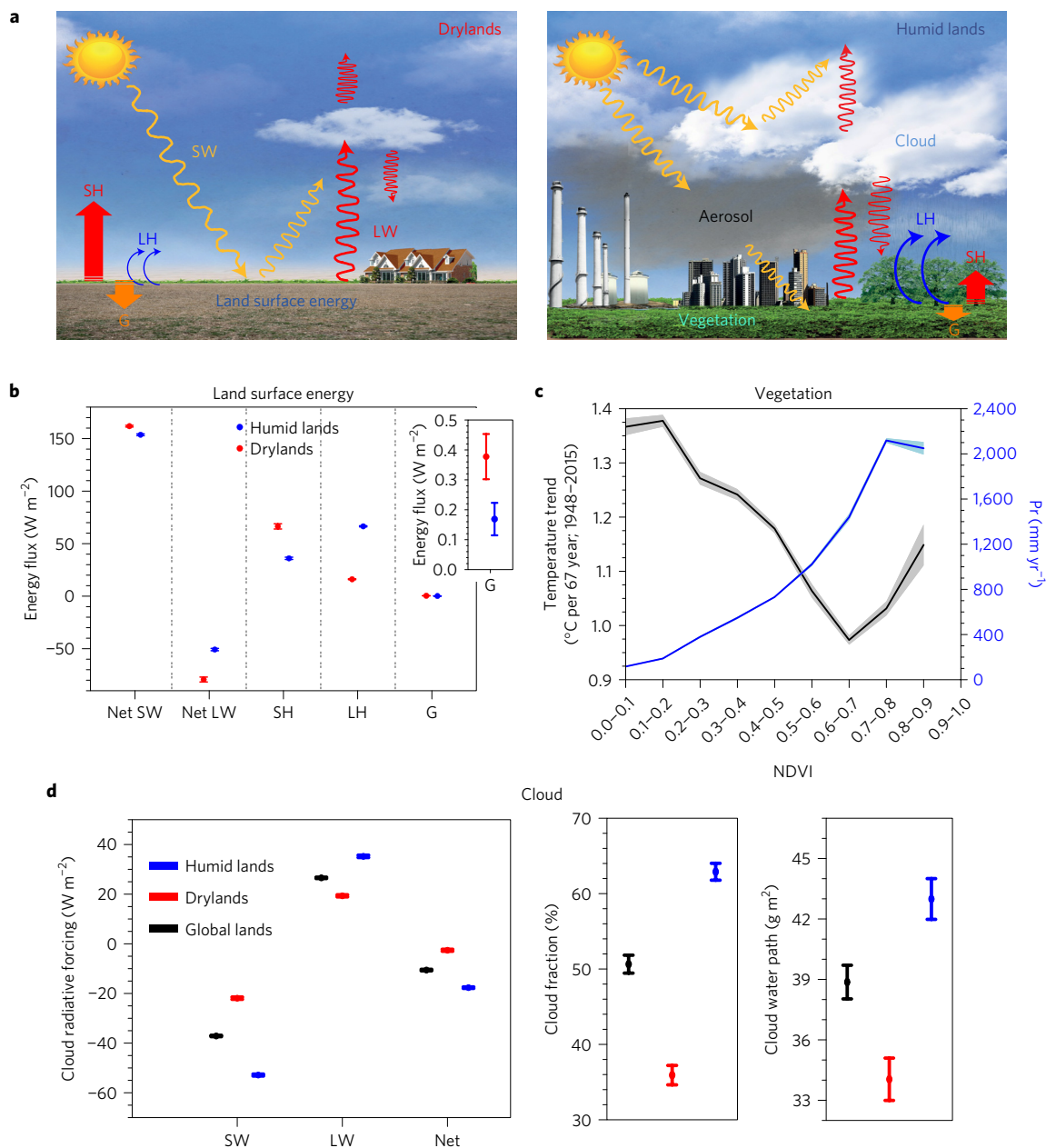


Figure 3 | The thermodynamic mechanisms of dryland-enhanced warming. **a**, Schematic diagram of local thermodynamic processes in drylands and humid lands. **b**, Comparison between the mean surface energy fluxes for drylands and humid lands based on GLDAS data, including net shortwave radiation (Net SW, downward positive), net longwave radiation (Net LW, downward positive), sensible heat flux (SH), latent heat flux (LH), and ground heat flux (G). The error bar denotes the ± 1 standard deviation range of temporal variations from 1948 to 2010. **c**, Variations in regionally averaged temperature trends over 1948–2015 (black) and climatological precipitation for 1948–2005 (blue) with respect to climatological (2001–2015) mean Normalized Difference Vegetation Index (NDVI). Shading denotes the ± 1 standard deviation range of the temporal variations in the NDVI for 2001 to 2015. **d**, The mean cloud radiative forcing, cloud fractions and liquid water paths during 2001–2015 averaged over drylands (red), humid lands (blue) and all land surfaces (black). The error bar denotes the ± 1 standard deviation range of temporal variations from 2001 to 2015.

global warming (about $-0.04 \text{ t ha}^{-1} \text{ yr}^{-1}$ or 1.1% compared with the 1971–1981 level), in contrast to the increases in the yields over humid lands, most of which exist in the humid lands of Europe (Fig. 4a). However, this increase is only temporary and the global maize yields would decrease by the latter part of the twenty-first century, when the negative effects of increasing evaporative demand and shortened growing season dominate²⁷. Total runoff (including surface and subsurface runoff) would decrease across all land surfaces, but most significantly in drylands with a GMSW from 1.5 °C to 2.0 °C (Fig. 4b), indicating that water shortage in drylands could become more severe. The P/PET ratio would

decrease across all land areas with a GMSW from 1.5 °C to 2.0 °C (Fig. 4c). This suggests that precipitation changes would not be sufficient to counterbalance the increased PET under rising temperatures, thereby resulting in increased risk of long-lasting drought over drylands and flash drought over humid lands²⁸. The climatic suitability for malaria transmission (Methods) would rise across all land surfaces, with the greatest increases occurring in drylands, from 19% to 27% higher than that of 1971–1981 with a GMSW of 1.5 °C to 2.0 °C (Fig. 4d). These impact evaluations show that dryland environments could be more vulnerable if GMSW were to increase from 1.5 °C to 2.0 °C.

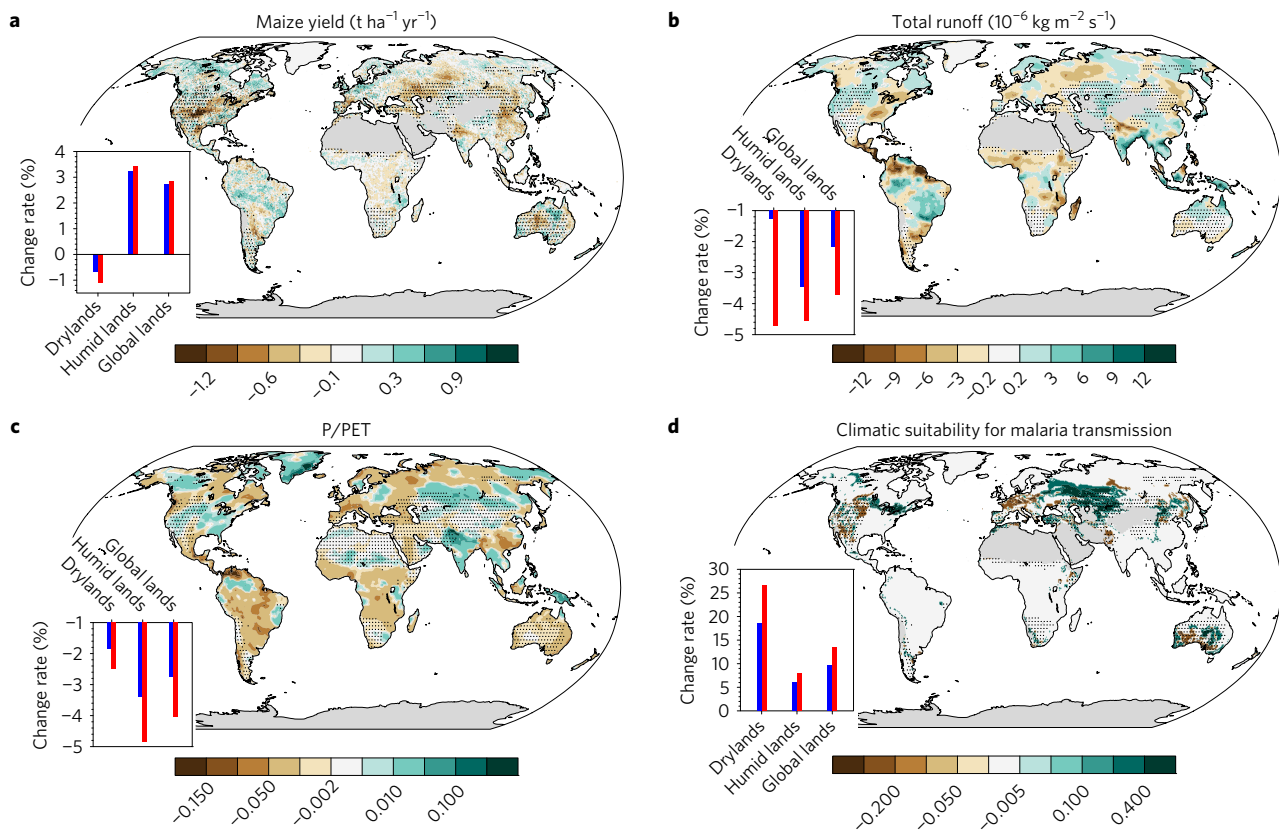


Figure 4 | Differences of climate change impact between the GMSW of 1.5 °C and 2.0 °C. **a–d**, Global distributions of future additional changes (the mean of the 11-year time slice when GMSW reaches 2.0 °C minus that of 1.5 °C case as shown in Supplementary Table 2) under the RCP8.5 for maize yields (**a**), total runoff (**b**), P/PET (**c**) and climatic suitability for malaria transmission (**d**) (see Methods). Grey shading denotes barren land or ice cover and the black points denote the defined drylands. The inserted graphs show percentage change rates for drylands, humid lands and all land surfaces (60° S–65° N) compared with historical mean values for 1971–1981 under a GMSW of 2.0 °C (red bars) and 1.5 °C (blue bars).

We emphasize that the above analyses were based on drylands defined using historical records. Several studies^{10,15,29,30} have shown that drylands could expand and become even drier under GHG-induced global warming conditions during the twenty-first century. This suggests that enhanced warming in drylands could affect an even larger population in the future¹⁰. Besides, under the given global-mean warming target, the global warming will affect most areas in the world, with some regions being more vulnerable than others. Contrasting drylands with humid lands is one of the ways to understand regional differences. For extreme temperature changes on a local scale, conditions would be more severe³. Thus, it is important to recognize these regional differences in setting up such a global-mean warming target.

In summary, we conclude that regional differences should be fully considered when discussing CO₂ emission reduction schemes, as humid (dry) lands have contributed ~58% (19%) of historical global CO₂ emissions, but the resultant warming has been 20–40% larger over drylands than humid lands; agricultural, hydrological and drought- and health-related risks are expected to increase substantially over drylands if the GMSW rises from 1.5 °C to 2.0 °C; a 1.5 °C GMSW target is necessary to limit mean dryland warming to 3.0 °C; and drylands should receive more attention when setting GMSW targets since they are most sensitive and vulnerable to GHG-induced climate change.

Methods

Methods, including statements of data availability and any associated accession codes and references, are available in the online version of this paper.

Received 7 October 2016; accepted 20 March 2017;
published online 24 April 2017

References

1. *Adoption of the Paris Agreement* FCCC/CP/2015/L9/Rev.1 (UNFCCC, 2015).
2. Knutti, R., Rogelj, J., Sedláček, J. & Fischer, E. M. A scientific critique of the two-degree climate change target. *Nat. Geosci.* **9**, 13–18 (2015).
3. Seneviratne, S. I., Donat, M. G., Pitman, A. J., Knutti, R. & Wilby, R. L. Allowable CO₂ emissions based on regional and impact-related climate targets. *Nature* **529**, 477–483 (2016).
4. Hartmann, D. L. *et al.* in *Climate Change 2013: The Physical Science Basis* (eds Stocker, T. F. *et al.*) 159–254 (IPCC, Cambridge Univ. Press, 2013).
5. Dai, A. Future warming patterns linked to today's climate variability. *Sci. Rep.* **6**, 19110 (2016).
6. Shukla, J. & Mintz, Y. Influence of land-surface evapotranspiration on the Earth's climate. *Science* **215**, 1498–1501 (1982).
7. Wu, Z., Huang, N., Wallace, J., Smoliak, B. & Chen, X. On the time-varying trend in global-mean surface temperature. *Clim. Dynam.* **37**, 759–773 (2011).
8. Wallace, J. M. & Johanson, C. M. Simulated versus observed patterns of warming over the extratropical northern hemisphere continents during the cold season. *Proc. Natl Acad. Sci. USA* **109**, 14337–14342 (2012).
9. Huang, J., Guan, X. & Ji, F. Enhanced cold-season warming in semi-arid regions. *Atmos. Chem. Phys.* **12**, 5391–5398 (2012).
10. Huang, J., Yu, H., Guan, X., Wang, G. & Guo, R. Accelerated dryland expansion under climate change. *Nat. Clim. Change* **6**, 166–171 (2016).
11. Guan, X. *et al.* Role of radiatively forced temperature changes in enhanced semi-arid warming in the cold season over East Asia. *Atmos. Chem. Phys.* **15**, 13777–13786 (2015).
12. Safriel, U. Deserts and desertification: challenges but also opportunities. *Land Degrad. Dev.* **20**, 353–366 (2009).
13. Taylor, K. E., Stouffer, R. J. & Meehl, G. A. An overview of CMIP5 and the experiment design. *Bull. Am. Meteorol. Soc.* **4**, 485–498 (2012).
14. Dai, A., Fyfe, J. C., Xie, S. & Dai, X. Decadal modulation of global surface temperature by internal climate variability. *Nat. Clim. Change* **5**, 555–559 (2015).

15. Feng, S. & Fu, Q. Expansion of global drylands under a warming climate. *Atmos. Chem. Phys.* **13**, 10081–10094 (2013).
16. North, B. G. R., Kim, K. Y., Shen, S. P. & Hardin, W. W. Detection of forced climate signals. Part I: Filter theory. *J. Clim.* **8**, 401–408 (1995).
17. Yin, D., Roderick, M. L., Leech, G., Sun, F. & Huang, Y. The contribution of reduction in evaporative cooling to higher surface air temperatures during drought. *Geophys. Res. Lett.* **41**, 7891–7897 (2014).
18. Foley, A. J., Costa, M. H., Delire, C., Ramankutty, N. & Snyder, P. Green surprise? How terrestrial ecosystems could affect Earth's climate. *Front. Ecol. Environ.* **1**, 38–44 (2003).
19. Liu, Z., Notaro, M., Kutzbach, J. & Liu, N. Assessing global vegetation-climate feedbacks from observations. *J. Clim.* **19**, 787–814 (2006).
20. Neelin, J., Chou, C. & Su, H. Tropical drought regions in global warming and El Niño teleconnections. *Geophys. Res. Lett.* **30**, 2275 (2003).
21. Hartmann, D. L., Ockert-Bell, M. E. & Michelsen, M. L. The effect of cloud type on Earth's energy balance: global analysis. *J. Clim.* **5**, 1281–1304 (1992).
22. Li, Z. *et al.* The long-term impacts of aerosols on the vertical development of clouds and precipitation. *Nat. Geosci.* **4**, 888–894 (2011).
23. Fu, Q., Johanson, C. M., Wallace, J. M. & Reichler, T. Enhanced mid-latitude tropospheric warming in satellite measurements. *Science* **312**, 1179 (2006).
24. Li, H., Dai, A., Zhou, T. & Lu, J. Responses of East Asian summer monsoon to historical SST and atmospheric forcing during 1950–2000. *Clim. Dynam.* **34**, 501–514 (2010).
25. Fu, C., Jiang, Z., Guan, Z., He, J. & Xu, Z. *Regional Climate Studies of China* Vol. 1, 156–159 (Springer, 2008).
26. Schleussner, C. F. *et al.* Differential climate impacts for policy-relevant limits to global warming: the case of 1.5 °C and 2 °C. *Earth Syst. Dynam.* **7**, 327–351 (2016).
27. Porter, J. R. *et al.* in *Climate Change 2014: Impacts, Adaptation, and Vulnerability* (eds Field, C. B. *et al.*) 485–533 (IPCC, Cambridge Univ. Press, 2014).
28. Wang, L., Yuan, X., Xie, Z., Wu, P. & Li, Y. Increasing flash droughts over China during the recent global warming hiatus. *Sci. Rep.* **6**, 30571 (2016).
29. Sherwood, S. & Fu, Q. A drier future? *Science* **343**, 737–739 (2014).
30. Berg, A. *et al.* Land–atmosphere feedbacks amplify aridity increase over land under global warming. *Nat. Clim. Change* **6**, 869–874 (2016).

Acknowledgements

This work was jointly supported by the National Science Foundation of China (41521004), the China University Research Talents Recruitment Program (111 project, No. B13045) and the foundation of Key Laboratory for Semi-Arid Climate Change of the Ministry of Education in Lanzhou University. A.D. is supported by the US National Science Foundation (Grant #AGS–1353740), the US Department of Energy's Office of Science (Award #DE–SC0012602), and the US National Oceanic and Atmospheric Administration (Award #NA15OAR4310086). The authors acknowledge the World Climate Research Programme's (WCRP) Working Group on Coupled Modelling (WGCM), the Global Organization for Earth System Science Portals (GO-ESSP) for producing the CMIP5 model simulations and making them available for analysis. The authors also acknowledge NOAA/OAR/ESRL PSD, Boulder, Colorado, USA, for providing NOAA Merged Air Land and SST Anomalies data and GPCC precipitation data from their website at <http://www.esrl.noaa.gov/psd>.

Author contributions

J.H. and H.Y. are first co-authors. J.H. designed the study and contributed to the ideas, interpretation and manuscript writing. H.Y. and A.D. contributed to the data analysis, interpretation and manuscript writing. H.Y. and Y.W. conducted the data processing. All of the authors discussed and reviewed the manuscript.

Additional information

Supplementary information is available in the [online version of the paper](#). Reprints and permissions information is available online at www.nature.com/reprints. Publisher's note: Springer Nature remains neutral with regard to jurisdictional claims in published maps and institutional affiliations. Correspondence and requests for materials should be addressed to J.H.

Competing financial interests

The authors declare no competing financial interests.

Methods

Observed surface air temperature. Three temperature data sets that were frequently used in the IPCC AR5 and other studies were included in this study. One is the Merged Land–Ocean Surface Temperature Analysis (MLOST) V3.5.4 developed by NOAA. MLOST is a global data set of monthly anomalies of air (over land) and sea surface (over ocean) temperatures from 1880 to the present on a 5° grid covering 87.5° S–87.5° N. It was derived from land temperature data from the Global Historical Climatology Network v3 (GHCN) and sea surface temperature (SST) data from the International Comprehensive Ocean–Atmosphere Data Set (ICOADS). The second data set is the Goddard Institute for Space Studies Surface Temperature (GISS) data set³¹ developed by NASA on a 2° grid and available from <http://data.giss.nasa.gov/gistemp>. It was derived from the NOAA GHCN v3 station data, ERSS2 v4 (ocean areas) and SCAR (Antarctic stations) data sets, and cover the period from 1880 to the present. The third set is the CRUTEM4 data set developed by the Met Office Hadley Centre and the Climatic Research Unit at the University of East Anglia³². CRUTEM4 is a data set on a 5° grid of surface air (over land) and sea surface (over ocean) temperature anomalies covering the period from 1850 to the present. To fill the missing values in the CRUTEM4, Dai and Zhao³³ have supplemented the CRUTEM4 with CRU TS2.3 temperature data, and this modified version of the CRUTEM4 was used here. All these data sets are for monthly temperatures, and we averaged them to derive the annual mean values analysed here.

Simulated surface air temperature. Model-simulated monthly surface air temperatures were drawn from 18 climate models participating in the Fifth Coupled Model Intercomparison Project (CMIP5)¹³ (Supplementary Table 1). The ensemble mean of these model outputs (one run from each model) was used to represent the externally forced temperature changes in this study. The all-forcing historical simulations (for 1861–2005) and projections (for 2006–2100) under the different Representative Concentration Pathways (RCPs, including RCP8.5, RCP6.0, RCP4.5, and RCP2.5) were used. When calculating temperature trends for 1920–2015 (Fig. 1), projections for 2006–2015 under the RCP4.5 were combined with corresponding historical simulations for 1920–2005. When referring to the 2.0 °C or 1.5 °C warming limitation, the 1861–1900 pre-industrial level was used²⁶ because it is commonly available for all CMIP5 models.

Observed precipitation. Two land precipitation data sets were used. One is the PREcipitation REConstruction over Land (PREC/L) data set³⁴ developed by the Climate Prediction Center (CPC), which is interpolated from station data from the Global Historical Climatology Network (GHCN) version 2 and Climate Anomaly Monitoring System (CAMS) data set for 1948 to the present on a 0.5° grid. For comparison, we also used the GPCC precipitation data set produced by the German Global Precipitation Climatology Centre. We used the Full Data Product (V7) for 1901 to 2010, which was based on quality-controlled raingauge data drawn from 67,200 stations worldwide that had 10 or more years of data³⁵.

Definition of drylands. Drylands are usually defined based on climatological precipitation (P) amount (with annual P < 600 mm) (ref. 9) or as regions where the ratio of precipitation to potential evapotranspiration (P/PET) is less than 0.65 (ref. 15). When mean precipitation is used, some cold areas in Siberia covered in frozen soils are classified as drylands because they receive low annual precipitation; however, these areas are classified as humid lands under the P/PET classification because of their low PET. Therefore, drylands are expanded using the precipitation classification, while humid lands are overestimated by the P/PET classification at northern high latitudes. Similarly, in some low-latitude areas, humid lands are overestimated by the precipitation classification because of high levels of precipitation over some dry areas, whereas drylands are overestimated by the P/PET classification because of high PET levels over some moist areas. Therefore, here we combine the precipitation and P/PET classifications to define typical drylands and humid lands. Latitudes were limited to 60° S–65° N to exclude effects of cold and frozen regions. We define areas with annual P < 600 mm and annual P/PET < 0.65 as drylands, and areas with annual P > 600 mm and annual P/PET > 0.65 as humid lands. The climatological mean was averaged from 1948 to 2005. The PET was calculated using the Penman–Monteith method^{36,37} as described by Feng and Fu¹⁵.

CO₂ emissions. The CO₂ emissions data used here were time series of annual CO₂ emissions from anthropogenic sources, including fossil-fuel burning, cement manufacturing and gas flaring in oil fields as well as energy production, consumption, and trade data, on a 1° × 1° grid from 1751 to 2013 drawn from the Carbon Dioxide Information Analysis Center (CDIAC)³⁸. Here, we analysed the 1920 to 2013 period, for which observational temperature data are widely available.

Estimating forced components and the amplification factor. The method used to separate external forced component from internal variability in observed temperature time series follows that of Dai and colleagues¹⁴. First, the mean of the whole analysis period (1920–2015) was removed to focus on the anomalies. All the

analyses were for annual mean temperature. The global-mean temperature anomaly time series of the CMIP5 ensemble mean was used to linearly regress the observed temperature time series at each grid point:

$$T(n, i) = b_F(i) \bar{T}_m(n) + T'(n, i) \tag{1}$$

where $T(n, i)$ is the surface temperature anomaly at grid point i for year n from observations and $n = 1, 2, \dots, 96$ for 1920, 1921, ..., 2015, respectively. $\bar{T}_m(n)$ is the global-mean surface air temperature anomaly for year n from the CMIP5 ensemble mean of historical simulations (for 1920–2005) and RCP4.5 projections (for 2006–2015). $b_F(i)$ is the regression slope at grid point i , and $b_F(i) \bar{T}_m(n)$ is defined as the externally forced component in the observations at grid point i for year n , and the residual $T'(n, i)$ is defined as the unforced component due to internal variability. Here, externally forced component averaged over the global (90° S–90° N) surfaces (including oceans) and the drylands is denoted by $\bar{T}_F^{\text{global}}(n)$ and $\bar{T}_F^{\text{dry}}(n)$, respectively, and the amplification factor of the externally forced component over drylands, A_{drylands}^F , is defined as

$$A_{\text{drylands}}^F = \frac{\bar{T}_F^{\text{dry}}(n)}{\bar{T}_F^{\text{global}}(n)} = \frac{\sum_{i=1}^{N_{\text{dry}}} b_F(i) \bar{T}_m(n) \cos \varphi_i / \sum_{i=1}^{N_{\text{dry}}} \cos \varphi_i}{\sum_{i=1}^{N_{\text{global}}} b_F(i) \bar{T}_m(n) \cos \varphi_i / \sum_{i=1}^{N_{\text{global}}} \cos \varphi_i} = \frac{\sum_{i=1}^{N_{\text{dry}}} b_F(i) \cos \varphi_i \cdot \sum_{i=1}^{N_{\text{global}}} \cos \varphi_i}{\sum_{i=1}^{N_{\text{global}}} b_F(i) \cos \varphi_i \cdot \sum_{i=1}^{N_{\text{dry}}} \cos \varphi_i} \tag{2}$$

where N_{global} and N_{dry} denote the number of grid points over the globe and the drylands, respectively, and φ_i is the latitude of grid i . Note that A_{drylands}^F does not depend on time. Furthermore, regional means of unforced temperature anomalies over drylands and over the globe are, respectively, denoted as

$$\bar{T}^{\text{dry}}(n) = \frac{\sum_{i=1}^{N_{\text{dry}}} T'(n, i) \cos \varphi_i}{\sum_{i=1}^{N_{\text{dry}}} \cos \varphi_i} \tag{3}$$

$$\bar{T}^{\text{global}}(n) = \frac{\sum_{i=1}^{N_{\text{global}}} T'(n, i) \cos \varphi_i}{\sum_{i=1}^{N_{\text{global}}} \cos \varphi_i} \tag{4}$$

where the amplification of the unforced component over the drylands, A_{drylands}^I , is defined as the regression slope between time series of $\bar{T}^{\text{dry}}(n)$ and $\bar{T}^{\text{global}}(n)$:

$$\bar{T}^{\text{dry}}(n) = A_{\text{drylands}}^I \bar{T}^{\text{global}}(n) \tag{5}$$

Here, the intercept is zero because the mean for the whole period has been removed. The amplification factors of other regions (humid lands, all land surfaces and oceans) are similarly derived. The estimated amplification factors for the unforced internal components of the three observational data sets are shown in Supplementary Fig. 7. The results show that the amplification factors of the unforced internal components differ less over different regions and are close to unity. For example, the unforced amplification factors using GISS temperature data for drylands, humid lands, lands and oceans are 1.01, 1.04, 1.08 and 1.01, respectively. This means that the unforced temperature signal is fairly uniform in spatial distribution.

The amplification of the raw observational anomalies over drylands, A_{drylands}^R , is defined by the following regression:

$$\bar{T}^{\text{dry}}(n) = A_{\text{drylands}}^R \bar{T}^{\text{global}}(n) \tag{6}$$

where $\bar{T}^{\text{drylands}}$ and \bar{T}^{global} denote regional mean temperature anomalies over the drylands and the globe, respectively:

$$\bar{T}^{\text{dry}}(n) = \frac{\sum_{i=1}^{N_{\text{dry}}} T(n, i) \cos \varphi_i}{\sum_{i=1}^{N_{\text{dry}}} \cos \varphi_i} \tag{7}$$

$$\bar{T}^{\text{global}}(n) = \frac{\sum_{i=1}^{N_{\text{global}}} T(n, i) \cos \varphi_i}{\sum_{i=1}^{N_{\text{global}}} \cos \varphi_i} \tag{8}$$

The amplification factors using the raw data are compared with those based on the estimated forced components, as shown in Supplementary Fig. 9. There is no significant difference between the two cases, which suggests that the contribution of the unforced component is small.

Reliability of deriving forced components from CMIP5 ensemble mean. In this study, the (nonlinear) time series of the forced global-mean temperature anomalies is derived from the CMIP5 18-model ensemble mean of all-forcing historical climate simulations. Nevertheless, the CMIP5 model-simulated forced changes contain errors due to model deficiencies and errors in historical forcing data. The reliability is discussed below.

As shown in Supplementary Fig. 10, the CMIP5 multi-model ensemble mean reproduces the observed global-mean temperature changes fairly well for 1920–2015. The correlation coefficient between the CMIP5 ensemble mean and the three observational data sets (GISS, CRUTEMP4 and MLOST) is 0.928, 0.932 and 0.924, respectively. This model-simulated response was re-scaled through regression with observations to account for the model bias, so that the overall global warming magnitude from 1920–2015 matches that in the observations.

Besides, it is found that the forced temperature (T) time series at each gridbox is highly correlated ($r > 0.95$) with the forced global-mean T series based on large ensemble simulations. Thus, the forced T series at each location can be represented by the forced global-mean T series (from the CMIP5 models) multiplied by a local scaling factor to reflect the different warming magnitudes at different locations. The re-scaling removes any mean bias in the model-simulated response to historical external forcing. The validation of this method has been presented¹⁴.

Different numbers of models in our estimates of this forced signal have also been tested and the results are very similar¹⁴. To apply a large ensemble as verifications, the results are tested with the ensemble mean of 64 all-forcing runs from 35 CMIP5 models to repeat the above procedures to derive the forced changes. The results (Supplementary Fig. 11) are similar to those in Fig. 2. There is little difference between the cases with 64 and 18 member ensembles.

Therefore, although the CMIP5 models are imperfect, their simulated temperature response to external forcing still represents our best estimate of forced T changes. Clearly, the results depend on how credible the model-simulated T response is.

Extending the historical amplification factor to the future. The CMIP5 models underestimate the historical warming over drylands; as shown in Fig. 1a, they are likely to underestimate the future warming over drylands as well. Therefore, we cannot use the model-projected future warming over drylands to estimate the amplification factor for the future climate.

The forced signal has the same temporal variations (although with different amplitudes) in the global-mean and dryland-mean temperature series (it is determined by the external forcing time series), see equation (2). Thus, the amplification factor is independent of time. As shown in Fig. 2a,b, a significant linear relationship between X and Y of the CMIP5 ensemble mean maintains from the historical period to future projections (with a correlation coefficient of >0.99), and the forced amplification factor is around 1.35 for drylands and 1.21 for humid lands. This means that the forced amplification factor from the observations would also be independent of time and could be expanded from the historical period to future projections if the forced component in observational data sets could be derived.

To verify whether the estimated forced amplification would be reliable for future projections, a sensitivity test is conducted. Supplementary Fig. 12 showed that the estimated amplification factor over drylands is fairly constant if data from 1920 to 2000 or later years were included. This suggests that the amplification factor estimated using data over 1920–2015 can be extended to future projections. This helps us correct the underestimation of the warming over drylands projected by the CMIP5 models for the future period.

Vegetation index. The Normalized Difference Vegetation Index (NDVI) data set³⁹ was derived from the MODIS Terra Vegetation Indices Monthly product MOD13C2 version 5 on a $1^\circ \times 1^\circ$ grid. Here, we used gridded annual-mean NDVI data from 2001 to 2015 to represent the mean vegetation density over a region. Negative values of the NDVI (values approaching -1) correspond to water surfaces. Values close to zero (-0.1 to 0.1) generally correspond to barren areas of rock, sand or snow. Finally, low positive values (approximately from 0.2 to 0.4) represent shrubland and grassland, and high values approaching 1.0 indicate temperate and tropical forests.

Energy flux on land surfaces. Surface energy flux data for shortwave and longwave radiation, sensible and latent heat, and ground heat were collected from the GLDAS land model simulation using the Noah Land Surface Model forced by observational data on a $1^\circ \times 1^\circ$ grid (GLDAS_NOAH10_M.2.0) for 1948 to 2010⁴⁰.

Cloud radiative effect. In this study, monthly averages of all-sky fluxes and clear-sky fluxes at the top of the atmosphere (TOA) from the CERES Energy Balanced and Filled (EBAF-TOA) Ed2.8 data set⁴¹ were used to assess cloud radiative effects (CRF). We computed 15-year averaged CRF data for January 2001–December 2015, following the standard methods used in previous studies⁴². First, shortwave (SW) and longwave (LW) CRFs were obtained by calculating the difference in radiation between clear-sky and all-sky conditions using following equations⁴³. The net CRF, which is the sum of SW and LW CRFs, was then determined.

$$\text{CRF}_{\text{SW}}(\text{TOA}) = (\text{SW}_{\text{all}}^{\downarrow} - \text{SW}_{\text{all}}^{\uparrow}) - (\text{SW}_{\text{clear}}^{\downarrow} - \text{SW}_{\text{clear}}^{\uparrow}) = \text{SW}_{\text{clear}}^{\uparrow} - \text{SW}_{\text{all}}^{\uparrow} \quad (9)$$

$$\text{CRF}_{\text{LW}}(\text{TOA}) = (\text{LW}_{\text{all}}^{\downarrow} - \text{LW}_{\text{all}}^{\uparrow}) - (\text{LW}_{\text{clear}}^{\downarrow} - \text{LW}_{\text{clear}}^{\uparrow}) = \text{LW}_{\text{clear}}^{\uparrow} - \text{LW}_{\text{all}}^{\uparrow} \quad (10)$$

$$\text{CRF}_{\text{Net}}(\text{TOA}) = \text{CRF}_{\text{SW}}(\text{TOA}) + \text{CRF}_{\text{LW}}(\text{TOA}) \quad (11)$$

In addition, cloud area fractions and liquid water paths from the SYN1deg Ed3A data set⁴⁴ were used to compare cloud properties over drylands and humid lands. We combined cloud retrievals from both the MODIS and CERES. Because the monthly data of cloud parameters from SYN1deg Ed3A end in November 2015, the averaged cloud fraction and liquid water path were computed for December 2000 to November 2015.

Aerosol optical depth (AOD). Moderate-resolution Imaging Spectroradiometer (MODIS) Level-3 Deep Blue AOD retrievals were used in this study. MODIS instruments aboard both the Terra and Aqua platforms have a high horizontal resolution (10 km), nearly global coverage, a wide spectral range (0.412–14.240 μm), and a high spectral resolution (36 channels). The data set (<https://ladsweb.nascom.nasa.gov/index.html>) is available on a $1^\circ \times 1^\circ$ grid at daily, eight-day and monthly temporal resolutions⁴⁵.

Climate impact assessment. Climate impacts of the 1.5 $^\circ\text{C}$ and 2 $^\circ\text{C}$ warming targets were assessed in terms of four sectors: agriculture (maize yield), hydrology (total runoff), drought (P/PET), and health (climatic suitability for malaria transmission). The impact data sets were based on projections drawn from the ISI-MIP Fast Track database⁴⁶ (<https://esg.pik-potsdam.de/search/ismip-ft>). The climate simulations were drawn from four bias-corrected CMIP5 models (GFDL-ESM2M, HadGEM2-ES, MIROC-ESM-CHEM, and NorESM1-M) with a spatial resolution of $0.5^\circ \times 0.5^\circ$ and a temporal range of historical simulations of 1971 to 2005, and the future projections are under RCP8.5 with a temporal range of 2006 to 2100. Supplementary Figs 14–16 show that the climate projections of these four models can well represent the ranges of the global mean temperature and precipitation of the other CMIP5 models, and the corresponding impact results are expected to be similar to those of the other CMIP5 models.

The 1.5 $^\circ\text{C}$ (2.0 $^\circ\text{C}$) warming condition was defined on the basis of projections in which the 11-year-smoothed mean annual temperature reaches the 1.5 $^\circ\text{C}$ (2.0 $^\circ\text{C}$) warming target relative to that of 1861–1900 for each climate model. Time slices of the climate model simulations using this definition are shown in Supplementary Table 2. There are different impact models for each sector, and the most frequently used impact models were chosen here. The model configuration is shown in Supplementary Table 3. The projected 1.5 $^\circ\text{C}$ (2.0 $^\circ\text{C}$) warming condition for the 11-year time slices was compared with the beginning of the simulation (1861–1900).

Climate suitability for malaria transmission. The model on climatic suitability for malaria transmission⁴⁷ was based on MARA/ARMA decision rules. This biological model defined a set of decision rules based on daily minimum and mean temperature constraints on the development of *Plasmodium falciparum* parasites and the Anopheles vector, and on precipitation constraints on mosquito survival and breeding capacities. Three variables were used to determine climatic suitability for a particular geographic location: monthly mean temperature, monthly mean of daily minimum temperatures, and total cumulative monthly precipitation. Detailed information on this approach can be found in Hartman and colleagues⁴⁷.

Data availability. The authors declare that the data supporting the findings of this study are available within the article and its Supplementary Information.

References

- Hansen, J., Ruedy, R., Stao, M. & Lo, K. Global surface temperature change. *Rev. Geophys.* **48**, RG4004 (2010).
- Morice, C. P., Kennedy, J. J., Rayner, N. A. & Jones, P. D. Quantifying uncertainties in global and regional temperature change using an ensemble of observational estimates: the HadCRUT4 dataset. *J. Geophys. Res.* **117**, D08101 (2012).
- Dai, A. & Zhao, T. Uncertainties in historical changes and future projections of drought. Part I: estimates of historical drought changes. *Climatic Change* <http://dx.doi.org/10.1007/s10584-016-1705-2> (2016).
- Chen, M. Y., Xie, P. P., Janowiak, J. E. & Arkin, P. A. Global land precipitation: a 50-yr monthly analysis based on gauge observations. *J. Hydrometeorol.* **3**, 249–266 (2002).
- Schneider, U. *et al.* *GPCC Full Data Reanalysis Version 7.0 at 0.5°: Monthly Land-Surface Precipitation from Rain-Gauges Built on GTS-Based and Historic Data* (Global Precipitation Climatology Centre, 2015); http://dx.doi.org/10.5676/DWD_GPCC/FD_M_V7_050
- Penman, H. L. Natural evaporation from open water, bare soil and grass. *Proc. R. Soc. Lond. A* **193**, 120–145 (1948).

37. Monteith, J. L. *Evaporation and Environment* 205–234 (Cambridge Univ. Press, 1965).
38. Andres, R. J., Boden, T. A. & Marland, G. *Annual Fossil-Fuel CO₂ Emissions: Mass of Emissions Gridded by One Degree Latitude by One Degree Longitude* (Carbon dioxide information analysis center, Oak Ridge National Laboratory, US Department of Energy, 2016); <http://dx.doi.org/10.3334/CDIAC/ffe.ndp058.2016>
39. Huete, A. *et al.* Overview of the radiometric and biophysical performance of the MODIS vegetation indices. *Remote Sens. Environ.* **83**, 195–213 (2002).
40. Rodell, M. *et al.* The Global Land Data Assimilation System. *Bull. Am. Meteorol. Soc.* **85**, 381–394 (2004).
41. Loeb, N. G. *et al.* Toward optimal closure of the Earth's top-of-atmosphere radiation budget. *J. Clim.* **3**, 748–766 (2009).
42. Ramanathan, V. *et al.* Cloud-radiative forcing and climate: results from the Earth Radiation Budget Experiment. *Science* **243**, 57–63 (1989).
43. Stanfield, R. E. *et al.* Assessment of NASA GISS CMIP5 and post-CMIP5 simulated clouds and TOA radiation budgets using satellite observations. Part II: TOA radiation budget and CREs. *J. Clim.* **28**, 1842–1864 (2015).
44. Wielicki, B. A. *et al.* Clouds and the Earth's Radiant Energy System (CERES): an Earth observing system experiment. *Bull. Am. Meteorol. Soc.* **77**, 853–868 (1996).
45. Sayer, A. M. *et al.* MODIS Collection 6 aerosol products: comparison between Aqua's e-Deep Blue, Dark Target, and “merged” data sets, and usage recommendations. *J. Geophys. Res.* **119**, 13965–13989 (2014).
46. Warszawski, L. *et al.* The Inter-Sectoral Impact Model Intercomparison Project (ISI-MIP): project framework. *Proc. Natl Acad. Sci. USA* **111**, 3228–3232 (2014).
47. Hartman, J., Ebi, K., McConnell, K., Chan, N. & Weyant, J. Climate suitability for stable malaria transmission in Zimbabwe under different climate change scenarios. *Glob. Change Hum. Health* **3**, 42–54 (2012).